



A robust asymmetrical contact algorithm for explicit solid dynamics

D. del Pozo^{1,2} · I. Lopez-Gomez³ · I. Romero^{1,2} 

Received: 22 May 2018 / Accepted: 29 October 2018
© Springer-Verlag GmbH Germany, part of Springer Nature 2018

Abstract

We describe a novel algorithm for the robust approximation of elastic, inelastic, and frictional contact problems in explicit computations. The method is based on a master-slave concept and a predictor/corrector split of the dynamic update. In the predictor step, the bodies move ignoring all contact interactions; in the correction, the nodes that have penetrated a body are pushed back while correcting their velocities to preserve linear momentum and balance the kinetic energy. In contrast with existing predictor/corrector contact algorithms, no iterations nor global computations are required in the correction step. Moreover, thanks to the geometrical basis of the method, the choice of an artificial penalty parameter is avoided. The contact algorithm does not require the computation of the normal vectors at the contacting surfaces, making it especially useful for simulations that employ finite element and certain meshfree discretizations, and for the simulation of contact among bodies with non-smooth boundaries.

Keywords Explicit integration · Contact · Predictor/corrector scheme · Finite elements · Meshfree methods

1 Introduction

Contact simulation is a key ingredient of Computational Solid Mechanics, one that is almost invariably employed for complex problems, especially in dynamics. Its ubiquitousness and the difficulties deriving from its non-smooth nature have prompted the publication of many different algorithmic approaches. Existing reviews [1–3] and monographs [4,5] classify the numerous works available on the topic, and attest to the relevance and difficulty of the problem, as well as the diversity of numerical approaches for its approximation.

In particular, dynamic contact is a central part of many nonlinear problems, including those involving ballistics, crashworthiness, metal forming, rolling, etc. The heterogeneity of applications has resulted in a wide range of algorithms that can be classified according to different criteria. In this work we focus on purely Lagrangian descriptions for solid bodies, where most of the literature is available (see, among many others, [6–13]).

A first crucial issue in the numerical treatment of contact is the overlap detection. In problems with multiple bodies, this step is very expensive in computational terms, and optimized search algorithms are absolutely necessary for large scale applications [10,11]. In these cases, moreover, parallel algorithms have been proposed to alleviate the overhead due to contact [12,14–16].

Implicit and explicit solutions of contact problems demand different strategies for the enforcement of the impenetrability condition. For fast processes, explicit algorithms are the methods of choice, and in this work we focus on them. Contact/impact algorithms for explicit integration are most often based on variations of the master-slave concept that goes back to the eighties [6,7]. In all these methods, the boundaries of the interacting bodies are discretized and their interpenetration is discouraged by means of carefully selected penalty forces whose magnitude, as a function of the penetration, is artificially selected [9,10,12–14]. Such a choice must strike a balance between a very stiff response that will effectively reduce the admissible time step size, and a very compliant one, which will not reproduce the impenetrability constraint properly.

Another option to enforce the impenetrability condition consists in using Lagrange multipliers, but this method cannot be applied directly in an explicit integration [5] because the diagonal form of the mass matrix is lost. To take advan-

✉ I. Romero
ignacio.romero@imdea.org

¹ Universidad Politécnica de Madrid, Madrid, Spain

² IMDEA Materials Institute, Eric Kandel, 2, Technogate,
28906 Madrid, Spain

³ California Institute of Technology, Pasadena, USA

tage of the exact impenetrability enforcement of the method of Lagrange multipliers, and to avoid the definition of artificial penalty parameters that might affect the stability of the time integration, modified strategies have been proposed. For example, some methods solve iteratively the global system of equations, including the contact constraints, until convergence [9,13,17,18]. Others, in order to speed up the computations, enforce locally the constraints, calculating the contact reactions (i.e., the Lagrange multipliers) in an iterative fashion [19] or explicitly, based only on geometric relations and balance principles [20]. The present work uses a predictor-corrector scheme of the latter type, hence completely avoiding the complex issue of artificial penalty selection and yielding a numerical method that is very robust. In addition, the method proposed has favorable properties from the energetic point of view that add to its robustness.

Methods based on master-slave contact models are intrinsically asymmetrical, due to the different roles played by the master and slave surfaces. A simple solution to avoid such a difference is to define twice each interacting pair, exchanging the master/slave roles in each of them. In this article we refrain from such a symmetrization, motivated by the potential application of the methods developed herein to numerical models that combine finite element and meshfree discretizations. These models are frequently employed together with explicit codes to calculate the solution of problems involving bodies that are severely distorted or even fragmented. This is the case of ballistics, mentioned before, but also crash simulations, structures under explosive loading, etc. In these situations, it is often advantageous to employ a mixed spatial discretization, one in which finite element models interact with meshfree bodies. Using such a combination, the meshfree parts can be employed to represent the components that are more severely distorted, while the finite element subdomains can model the rest, combining the advantages of meshfree methods to accommodate large distortions, and the efficiency of finite elements [21–24]

From the point of view of contact, however, the key issue is not whether the interacting bodies of a model are discretized with finite elements or a meshfree method, but rather if their boundaries are well defined, as in a finite element mesh, but not in a meshfree or particle representation. Contact algorithms that need to compute the surface normals at contact points run into difficulties when dealing with meshfree discretizations which, strictly speaking, do not define this vector field at every boundary point. The method presented in this work does not require the calculations of the normal vectors to the interacting surfaces. This, first, allows for a simple contact definition between meshfree and finite element discretizations. Additionally, it can model, without any modification, contact among bodies with non-smooth boundaries.

In this article we will use examples that combine the two types of spatial discretizations, but the method is directly applicable to models based only on finite elements, where the asymmetry of the contact interaction could be reversed, if desired, as in other standard implementations.

The rest of the article has the following structure. In Sect. 2 we briefly summarize the governing equations of dynamic contact. Section 3 discusses the spatial discretization of the problem. The new contact algorithm is described in Sect. 4 where elastic, inelastic, and frictional cases are considered. In addition to the algorithmic details, proofs of energy conservation/dissipation are provided for each model. The simulations of Sect. 5 illustrate the features of the method using mixed finite element/meshfree examples, and the article is closed in Sect. 6 with a summary of the most relevant results.

2 Problem description

We briefly recall the governing equations of a problem with multiple deformable bodies, possibly interacting among them through frictionless contact. More complex contact interactions will be considered in the numerical methods of Sect. 4, but we limit the theoretical exposition to the frictionless case for simplicity.

Each of the bodies considered in the problem will be referred to as \mathcal{B}_i , with $i = 1, \dots, N$, corresponding to an open subset of \mathbb{R}^3 with boundary $\partial\mathcal{B}_i$. Points on any of the bodies are denoted as \mathbf{x} and we assume the existence of N deformations $\varphi_i : \mathcal{B}_i \times [0, T] \rightarrow \mathbb{R}^3$. To formulate the contact problem, we employ the notion of distance between bodies defined as

$$d(\mathcal{B}_i, \mathcal{B}_j) = \inf_{\mathbf{x} \in \varphi_i(\mathcal{B}_i)} \inf_{\mathbf{y} \in \varphi_j(\mathcal{B}_j)} |\mathbf{x} - \mathbf{y}|. \tag{1}$$

In addition, it is important to partition the boundary $\partial\mathcal{B}_i$ of each body into disjoint subsets $\Gamma_i^t, \Gamma_i^\varphi, \Gamma_{ij}^c$ referring to the boundary with Neumann conditions, Dirichlet conditions, and contact forces, respectively, which satisfy

$$\partial\mathcal{B}_i = \overline{\Gamma_i^t \cup \Gamma_i^\varphi \cup \bigcup_{j=1}^N \Gamma_{ij}^c}. \tag{2}$$

Then, the problem is formulated as:

$$\begin{aligned} \text{Div } \mathbf{P} + \rho_0 \mathbf{B} &= \rho_0 \ddot{\varphi}_i && \text{in } \mathcal{B}_i \\ \varphi_i &= \bar{\varphi}_i && \text{on } \Gamma_i^\varphi \\ \mathbf{P} \mathbf{N}_i &= \bar{\mathbf{T}}_i && \text{on } \Gamma_i^t \\ \mathbf{P} \mathbf{N}_i &= -p_{ij} \mathbf{N}_i && \text{on } \Gamma_{ij}^c \end{aligned} \tag{3}$$

where Div is the material divergence, \mathbf{P} the first Piola-Kirchhoff stress tensor, ρ_0 the reference density, \mathbf{B} the volumetric force, $\bar{\varphi}_i$ a surface field of known deformations,

\bar{T}_i the known tractions, N_i the normal field to the body, and p_{ij} the contact pressure of the j th body on the i th one. These contact pressures satisfy

$$p_{ij} \geq 0, \quad p_{ij} d(\mathcal{B}_i, \mathcal{B}_j) = 0, \quad p_{ij} = p_{ji}. \tag{4}$$

The goal of this work is to present a numerical method for the space and time discretization of Eqs. (3) and (4). Such an approximation is fairly standard in the absence of contact interactions. However, the numerical treatment of the complementary conditions (4) greatly complicates the global problem.

3 Spatial discretization

We start by considering a spatial discretization of the bodies $\{\mathcal{B}_i\}_{i=1}^N$. The methods later introduced are general enough to encompass both finite element and meshfree discretizations. However, they are limited by the constraint that at least one of the discretized bodies in each contact interaction must have a well-defined boundary. In practice, this means that even though bodies can be discretized in space with a mesh or particle-based method, each pairwise contact interaction must involve at least one meshed body.

The key classification of the contacting bodies is thus between those that possess a mesh and those that not, and we refer to these sets, respectively, as \mathcal{F} and \mathcal{M} . For either type, we assume henceforth that we can define an approximation of every scalar, vector, or tensor field f on \mathcal{B}_i , denoted f^h , and defined as

$$f(\mathbf{X}) \approx f^h(\mathbf{X}) = \sum_{\alpha} N_{i,\alpha}(\mathbf{X}) c_{i,\alpha}. \tag{5}$$

The scalar functions $N_{i,\alpha} : \mathcal{B}_i \rightarrow \mathbb{R}$ are the standard finite element shape functions, if the body is discretized with a mesh, or some meshfree interpolation function if not. In either case, the scalars $c_{i,\alpha}$ are simply the weights in the linear combination (5).

We briefly describe the key features of the two types of spatial discretizations considered in the current work.

3.1 Finite element discretization

A body $\mathcal{B}_i \in \mathcal{F}$ is discretized with finite elements by defining a node set \mathcal{N}_i and a triangulation \mathcal{T}_i of tetrahedra or hexahedra. This triangulation partitions the domain into disjoint elements $e_i^\alpha \subset \mathcal{B}_i$ with vertices $n_i^\alpha \in \mathcal{N}_i$ and allows to construct piecewise polynomial functions $N_{i,\alpha}$ with the property $N_{i,\alpha}(n_i^\gamma) = \delta_{\alpha\gamma}$, where $\delta_{\alpha\gamma}$ refers to the Kronecker delta. The support of the function $N_{i,\alpha}$ is the set $\cup_{e_i^\beta \ni n_i^\alpha} e_i^\beta$.

3.2 Meshfree discretization

Let $\mathcal{B}_i \in \mathcal{M}$, and define a finite node set $\mathcal{N}_i = \{n_i^\alpha\}$ on this domain. By definition, there might be a mesh defined on \mathcal{B}_i or not, but we will never make reference to it. The only condition on the discretization of this body is that there exists a collection of approximation functions $N_{i,\alpha} : \mathcal{B}_i \rightarrow \mathbb{R}$ such that linear combinations of the type (5) can be employed to approximate the deformation and velocity of the body. In what follows, we refer to bodies in \mathcal{M} as *meshfree* bodies to indicate that there is no need for a mesh to be defined on them, although they might have it.

There is much freedom in the choice of these functions. As stated before, they might be finite element shape functions if the body has a mesh, but can also be any meshfree function including those employed in the element free Galerkin method, the natural neighbor method, or any other of this sort (see, e.g. [25], for a review).

For the kind of explicit computations considered in the current work, meshfree methods based on approximation functions that possess the Kronecker’s delta property greatly simplify the contact implementation. Not all meshfree method satisfy this condition, but approximations such as the ones defined in the natural element method [26], and the local maximum entropy functions with log-distance [27], verify the Kronecker’s delta property. Meshfree discretizations with local finite element enrichments can also be employed to this goal [23,28]. In the derivations that follow we will assume that the meshfree discretizations of the bodies in \mathcal{M} are interpolatory and, in particular, in Sect. 5 we will employ local maximum entropy functions.

3.3 Semi-discrete equations of motion

When a Galerkin type method is employed to approximate the balance of linear momentum equation in all the bodies of the model, irrespective of the discretization strategy chosen, a system of semi-discrete equations is obtained with the standard form. In particular, for the i th body this ordinary differential equation reads

$$\begin{aligned} & \int_{\mathcal{B}_i} \rho_0 \ddot{\varphi}_i^h \cdot \eta^h \, dV + \int_{\mathcal{B}_i} \mathbf{P} \cdot \text{Grad } \eta^h \, dV \\ &= \int_{\mathcal{B}_i} \rho_0 \mathbf{B} \cdot \eta^h \, dV + \int_{\Gamma_i^t} \bar{T}_i \cdot \eta^h \, dA \\ & \quad - \sum_j \int_{\Gamma_{ij}^c} p_{ij} N_i \cdot \eta^h \, dA, \end{aligned} \tag{6}$$

where $\eta^h : \mathcal{B}_i \rightarrow \mathbb{R}^3$ is an arbitrary weighting function in the finite element or meshfree space. We note that these equations are completely identical, except for the last term accounting for the contact interactions, to the equations of

motion in nonlinear dynamics. Associated to these interactions, conditions (4) need to be employed to calculate the contact pressure.

Selecting the test function η^h to be of the form $\eta^h = N_{i,\alpha} \mathbf{c}$, with $n_i^\alpha \in \mathcal{N}_i$ and $\mathbf{c} \in \mathbb{R}^3$, the equations of motion in matrix form follow

$$\begin{aligned} \mathbf{M}^i \ddot{\Phi}^i + \mathbf{f}_{int}^i &= \mathbf{f}_{ext}^i, \\ \mathbf{f}_{int}^{i,\alpha} &= \int_{\mathcal{B}_i} \mathbf{P} \text{Grad } N_{i,\alpha} \, dV, \\ \mathbf{f}_{ext}^{i,\alpha} &= \int_{\mathcal{B}_i} \rho_0 \mathbf{B} N_{i,\alpha} \, dV + \int_{\Gamma_i^t} \bar{\mathbf{T}}_i N_{i,\alpha} \, dA \\ &\quad - \sum_j \int_{\Gamma_{ij}^c} p_{ij} N_i N_{i,\alpha} \, dA, \end{aligned} \quad (7)$$

where Φ^i , \mathbf{f}_{int}^i , \mathbf{f}_{ext}^i are the vectors collecting, respectively, the nodal deformations, internal forces, and external forces. The matrix \mathbf{M}^i is the mass matrix of body \mathcal{B}_i which, in order to later obtain an explicit method, is lumped into diagonal form. In other words, the (i, j) component in the block relating nodes α and β is

$$M_{\alpha\beta}^{ij} = m^{i,\alpha} \delta_{\alpha\beta} \delta_{ij}, \quad (8)$$

with $m^{i,\alpha}$ the mass of node n_i^α .

4 Time integration and contact algorithm

The semi-discrete equations (6) are next integrated in time with an explicit algorithm. The main idea of the proposed method is to use a predictor-corrector scheme: first we integrate the equations of motion using the central difference method, ignoring all possible contacts; then, we correct the positions and velocities to account for the pairwise interactions.

To define the integration, we select $M + 1$ instants $t_n = n \Delta t$, with $n = 0, 1, \dots, M$, where $\Delta t = T/M$ is the time step size, assumed for simplicity to be constant. Then, we define the approximations to the deformations, material velocities, and material acceleration, respectively, at each node and time t_n to be $\varphi_n^{i,\alpha}$, $\mathbf{v}_n^{i,\alpha}$, $\mathbf{a}_n^{i,\alpha}$, where the index i runs through all body labels and α through the node set in each body. Following the standard notation, we will refer to $f_{n+\gamma}$ as the convex combination $(1 - \gamma)f_n + \gamma f_{n+1}$ for any nodal variable f , and $\gamma \in [0, 1]$.

Collecting the nodal deformations into a global vector Φ_n , we can postulate a *predictor* state as given by the nodal updates

$$\begin{aligned} \tilde{\mathbf{a}}^{i,\alpha} &= (m^{i,\alpha})^{-1} \left(\tilde{\mathbf{f}}_{ext}^{i,\alpha}(\Phi_{n-1/2}) - \mathbf{f}_{int}^{i,\alpha}(\Phi_{n-1/2}) \right), \\ \tilde{\mathbf{v}}^{i,\alpha} &= \mathbf{v}_n^{i,\alpha} + \Delta t \tilde{\mathbf{a}}^{i,\alpha}, \\ \tilde{\varphi}^{i,\alpha} &= \varphi_n^{i,\alpha} + \Delta t \tilde{\mathbf{v}}^{i,\alpha}. \end{aligned} \quad (9)$$

where $\tilde{\mathbf{f}}_{ext}^{i,\alpha}$ refers to the nodal external force defined in Eq. (7), but ignoring the contributions due to contact interactions. We note that, as in the standard central difference method, the predictors $\tilde{\varphi}^{i,\alpha}$ and $\tilde{\mathbf{v}}^{i,\alpha}$ refer to quantities at time t_{n+1} while $\tilde{\mathbf{a}}^{i,\alpha}$ is an approximation to the acceleration at time $t_{n+1/2}$.

After the positions of the bodies have been *predicted* using the central difference method, these are *corrected* to account for possible penetrations. The latter result in tractions on the contacting surfaces which in turn cause the exchange of momenta and energy.

4.1 Contact detection

Before any contact modeling can be done, the overlap of bodies in the predicted solution must be detected. Obviously, if there is no overlap, this predicted solution needs not be corrected and the integration step can proceed as in free body dynamics.

The focus of this article is on the modeling and simulation of contact interactions between bodies discretized with a mesh structure and others without it. Thus, for simplicity, we consider next only the analysis of the potential contact between a body $\mathcal{B}_i \in \mathcal{F}$ and a second one $\mathcal{B}_j \in \mathcal{M}$ as depicted in Fig. 1. We assume also, for simplicity, that the body \mathcal{B}_i does not crack or break during the simulation, and thus its boundary remains unchanged. We note, however, that this choice is not due to any limitation of the contact algorithm itself.

We note that only \mathcal{B}_i has a well-defined boundary, and thus contact detection algorithms between these two bodies are not symmetric. On \mathcal{B}_i we can hence define the *skin* as the element set

$$S_i = \bigcup_{e_i^\alpha \cap \partial \mathcal{B}_i \neq \emptyset} e_i^\alpha \quad (10)$$

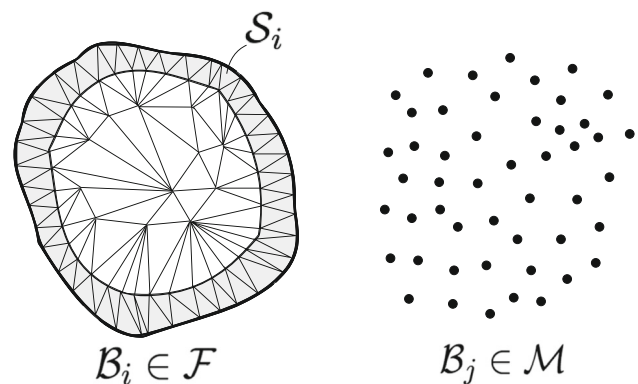


Fig. 1 The two types of bodies considered are meshed (left) and mesh-free (right). Bodies with a mesh have a well-defined *skin* of elements intersecting the boundary

with nodes

$$\Sigma_i = \mathcal{N}_i \cap \mathcal{S}_i. \tag{11}$$

From the computational point of view it is important to realize that the *skin* typically contains far fewer elements than the body \mathcal{B}_i itself.

The *skin* will be used to monitor potential penetrations of the meshfree body into the space occupied by the finite element body. In our computations, we simply verify in an exhaustive fashion if the predicted position of any of the nodes on the surface of \mathcal{B}_j falls within Σ_i . To ensure that the predicted positions $\tilde{\varphi}^{j,\beta}$ do not fall within the body \mathcal{B}_i and beyond its *skin*, we must restrict the time step size to be

$$\Delta t = \min \left(\Delta t_{CFL}, \frac{h_i}{V_i + V_j} \right). \tag{12}$$

In this expression Δt_{CFL} is the time step size as dictated by the CFL condition in the deformable bodies, h_i is the minimum element size in the skin \mathcal{S}_i , and V_i, V_j are the largest moduli of the velocity vectors in the two contacting bodies.

When the time step size in the integration scheme is selected according to Eq. (12), the predicted position of the node $n_j^\beta \in \mathcal{N}_j$ can be either outside the skin of \mathcal{B}_i , on its surface, or inside it. In the first two situations there is no violation of the inter-penetrability constraint, and thus the predicted position, velocity, and acceleration of the nodes $n_i^\alpha \in \mathcal{N}_i$ and $n_j^\beta \in \mathcal{N}_j$ can be taken as the correct one for the update and thus

$$\begin{aligned} (\varphi_{n+1}^{i,\alpha}, \mathbf{v}_{n+1}^{i,\alpha}, \mathbf{a}_{n+1/2}^{i,\alpha}) &= (\tilde{\varphi}^{i,\alpha}, \tilde{\mathbf{v}}^{i,\alpha}, \tilde{\mathbf{a}}^{i,\alpha}), \\ (\varphi_{n+1}^{j,\beta}, \mathbf{v}_{n+1}^{j,\beta}, \mathbf{a}_{n+1/2}^{j,\beta}) &= (\tilde{\varphi}^{j,\beta}, \tilde{\mathbf{v}}^{j,\beta}, \tilde{\mathbf{a}}^{j,\beta}). \end{aligned} \tag{13}$$

4.2 Correction geometry

We study next the correction update for the nodes $n_j^\beta \in \mathcal{N}_j$, with $\mathcal{B}_j \in \mathcal{M}$, and $n_i^\alpha \in \Sigma_i$ when the predictor update has placed n_j^β inside the *skin* \mathcal{S}_i , that is, $\tilde{\varphi}^{j,\beta} \in \varphi_i(\mathcal{S}_i)$. In such situations we need, first, to define a correction direction \mathbf{n} , with $|\mathbf{n}| = 1$, which will be used to move the predicted position away from the interior of \mathcal{B}_i . The definition of such vector is not trivial because it must be defined for convex and concave polygonal bodies, and certain obvious definitions, such as the direction towards the closest point projection on the boundary, might not be well-defined.

For a general meshed domain \mathcal{B}_i , if the node $n_j^\beta \in \mathcal{N}_j$, with $\mathcal{B}_j \in \mathcal{M}$, at its predicted position is inside $\varphi_i(\mathcal{S}_i)$, then there must exist at least one element $e_i^\alpha \in \mathcal{S}_i$ such that $n_j^\beta \in e_i^\alpha$ (See Fig. 2). For three dimensional problems, the

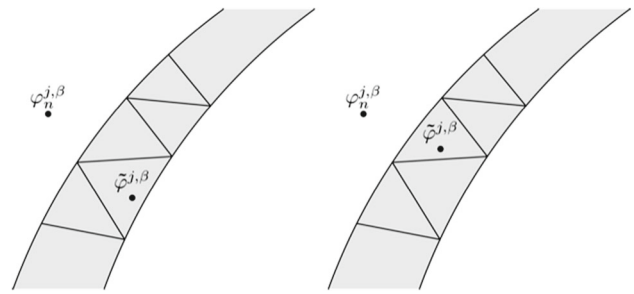


Fig. 2 Two types of *skin* penetration in plane problems

element e_i^α must have a face, an edge, or a vertex on $\partial\mathcal{B}_i$, and the computation of the correction direction is different in the three situations.

The correction that needs to be performed after a penetration has been detected can be split in two steps. First, the node in the meshfree body must be moved onto the surface of the skin. Second, an exchange of linear momentum must be accounted for between this node and those in the element e_i^α .

We address first the position correction. For any type of finite element body, be it convex or concave, we define the corrected position to be

$$\varphi_{n+1}^{j,\beta} = \arg \min_{x \in e_i^\alpha \cap \partial\mathcal{B}_i} |\tilde{\varphi}^{j,\beta} - \mathbf{x}|, \tag{14}$$

noting that, for simplicial meshes, the set $e_i^\alpha \cap \partial\mathcal{B}_i$, which might be a triangle, and edge, or a vertex, is always convex, and thus the minimization problem in (14) has always a unique solution. If the finite element mesh of the body \mathcal{B}_i is not simplicial, this minimization might have more than one solution. In this case the corrected position is taken to be any of them.

Once the corrected position of the node has been obtained, an exchange of momentum is applied onto this same node and the nodes of the element e_i^α . For that, an update direction needs to be defined which, irrespective of the smoothness of the surface at the projection point can always be defined as

$$\mathbf{n} = \frac{\varphi_{n+1}^{j,\beta} - \tilde{\varphi}^{j,\beta}}{|\varphi_{n+1}^{j,\beta} - \tilde{\varphi}^{j,\beta}|}. \tag{15}$$

4.3 Correction forces

The node $n_j^\beta \in \mathcal{N}_j$ that has penetrated the *skin* and the element $e_i^\alpha \in \mathcal{B}_i$ must exchange linear momentum to correct their trajectories. More specifically, we identify the set $\sigma_i^\alpha = \{n_i^\gamma \in e_i^\alpha \cap \partial\mathcal{B}_i\}$ of nodes in the finite element that receive an impulse due to the contact. In addition, we assume that the node n_j^β and the nodes in σ_i^α have masses, denoted respectively as m_j^β and m_i^γ , obtained by lumping their corresponding element or meshfree contributions, as explained in

Sect. 3. Using these lumped masses we define the momenta of the nodes at time t_{n+1} as

$$\mathbf{p}_{n+1}^{j,\beta} = m_j^\beta \mathbf{v}_{n+1}^{j,\beta}, \quad \mathbf{p}_{n+1}^{i,\gamma} = m_i^\gamma \mathbf{v}_{n+1}^{i,\gamma}, \quad (16)$$

and use the notation $\tilde{\mathbf{p}}^{j,\beta}, \tilde{\mathbf{p}}^{i,\gamma}$ for the predicted values. The kinetic energy of the nodes will be denoted as $K_{n+1}^{j,\beta}$, etc., and defined as

$$K_{n+1}^{j,\beta} = \frac{1}{2} m_j^\beta |\mathbf{v}_{n+1}^{j,\beta}|^2, \quad K_{n+1}^{i,\gamma} = \frac{1}{2} m_i^\gamma |\mathbf{v}_{n+1}^{i,\gamma}|^2, \quad (17)$$

again with $\tilde{K}^{j,\beta}, \tilde{K}^{i,\gamma}$ referring to the predicted values.

Let us consider, for the moment, a frictionless contact with perfect energy restitution. Given the position and velocity of nodes $n_j^\beta \in \mathcal{B}_j$ and $n_i^\gamma \in \sigma_i^\alpha$ at the predictor step, and the unit vector \mathbf{n} defined in Eq. (15), to compute their corrected velocities we impose the following balance equations:

$$\mathbf{p}_{n+1}^{j,\beta} - \tilde{\mathbf{p}}^{j,\beta} = \lambda^{j,\beta} \mathbf{n}, \quad (18a)$$

$$\mathbf{p}_{n+1}^{i,\gamma} - \tilde{\mathbf{p}}^{i,\gamma} = -\lambda^{i,\gamma} \mathbf{n}, \quad (18b)$$

$$\mathbf{p}_{n+1}^{j,\beta} + \sum_{\gamma|n_i^\gamma \in \sigma_i^\alpha} \mathbf{p}_{n+1}^{i,\gamma} = \tilde{\mathbf{p}}^{j,\beta} + \sum_{\gamma|n_i^\gamma \in \sigma_i^\alpha} \tilde{\mathbf{p}}^{i,\gamma}, \quad (18c)$$

$$K_{n+1}^{j,\beta} + \sum_{\gamma|n_i^\gamma \in \sigma_i^\alpha} K_{n+1}^{i,\gamma} = \tilde{K}^{j,\beta} + \sum_{\gamma|n_i^\gamma \in \sigma_i^\alpha} \tilde{K}^{i,\gamma}. \quad (18d)$$

Equations (18a) and (18b) express the changes in linear momentum in the involved nodes at impact. Equations (18c) and (18d) enforce the conservation of total linear momentum and kinetic energy, respectively. The system of equations (18) must be solved to find the updated velocities in the nodes and the impulses $\lambda^{j,\beta}, \lambda^{i,\gamma}$ which, if there is to be a physically realistic impact, must be non-negative. However, this system is, in general, undetermined. To see this, let us first note that the components of the linear momenta that are orthogonal to \mathbf{n} are conserved. Given any vector \mathbf{m} such that $\mathbf{n} \cdot \mathbf{m} = 0$, from Eqs. (18a) and (18b) we obtain

$$\mathbf{p}_{n+1}^{j,\beta} \cdot \mathbf{m} = \tilde{\mathbf{p}}^{j,\beta} \cdot \mathbf{m}, \quad (19a)$$

$$\mathbf{p}_{n+1}^{i,\gamma} \cdot \mathbf{m} = \tilde{\mathbf{p}}^{i,\gamma} \cdot \mathbf{m}. \quad (19b)$$

Hence, if M is the number of nodes in σ_i^α , the system (18) can be reduced to a system of $M + 3$ scalar equations

$$\mathbf{p}_{n+1}^{j,\beta} |_{\mathbf{n}} - \tilde{\mathbf{p}}^{j,\beta} |_{\mathbf{n}} = \lambda^{j,\beta}, \quad (20a)$$

$$\mathbf{p}_{n+1}^{i,\gamma} |_{\mathbf{n}} - \tilde{\mathbf{p}}^{i,\gamma} |_{\mathbf{n}} = -\lambda^{i,\gamma}, \quad (20b)$$

$$\mathbf{p}_{n+1}^{j,\beta} |_{\mathbf{n}} + \sum_{\gamma|n_i^\gamma \in \sigma_i^\alpha} \mathbf{p}_{n+1}^{i,\gamma} |_{\mathbf{n}} = \tilde{\mathbf{p}}^{j,\beta} |_{\mathbf{n}} + \sum_{\gamma|n_i^\gamma \in \sigma_i^\alpha} \tilde{\mathbf{p}}^{i,\gamma} |_{\mathbf{n}} \quad (20c)$$

$$K_{n+1}^{j,\beta} + \sum_{\gamma|n_i^\gamma \in \sigma_i^\alpha} K_{n+1}^{i,\gamma} = \tilde{K}^{j,\beta} + \sum_{\gamma|n_i^\gamma \in \sigma_i^\alpha} \tilde{K}^{i,\gamma} \quad (20d)$$

where the notation $(\cdot)|_{\mathbf{n}}$ denotes the projection of a vector onto the direction \mathbf{n} . In this system there are $2M + 2$ unknowns, namely, the $M + 1$ components of the linear momenta at the corrected step in the direction of \mathbf{n} , and the $M + 1$ impulses. The system has a unique solution only when $M = 1$. We propose next a *contact model* that provides $M - 1$ additional equations and allows to solve the update for an arbitrary number of nodes in the contacting surface. First, let us note that Eq. (20c) can be rewritten as

$$\lambda^{j,\beta} = \sum_{\gamma|n_i^\gamma \in \sigma_i^\alpha} \lambda^{i,\gamma}. \quad (21)$$

Then, let us define the barycentric coordinates of the projection $\boldsymbol{\varphi}_{n+1}^{j,\beta}$, that is, the scalars $\chi^{i,\gamma} \geq 0$ such that

$$\boldsymbol{\varphi}_{n+1}^{j,\beta} = \sum_{\gamma|n_i^\gamma \in \sigma_i^\alpha} \chi^{i,\gamma} \tilde{\boldsymbol{\varphi}}^{i,\gamma}, \quad (22)$$

with $\sum_{\gamma|n_i^\gamma \in \sigma_i^\alpha} \chi^{i,\gamma} = 1$, noting that the projected position depends only on the predictors. In view of the well-posedness of projection (14) the coordinates are unique. The contact model proposed apportions the impulse $\lambda^{j,\beta}$ to the nodes on σ_i^α according to these barycentric coordinates, that is,

$$\lambda^{i,\gamma} = \chi^{i,\gamma} \lambda^{j,\beta}, \quad (23)$$

providing $M - 1$ additional equations that close the system (20).

4.4 Velocity solution algorithm

The final step in the contact update is the solution of the system of equations (20). A closed form expression for the impulses and velocities at the predicted step can be found as follows. An algebraic manipulation shows that the energy balance (20d) can be written as

$$0 = \sum_{\gamma|n_i^\gamma \in \sigma_i^\alpha} \left(\frac{(\lambda^{i,\gamma})^2}{2m_i^\gamma} - \lambda^{i,\gamma} \tilde{\mathbf{v}}^{i,\gamma} \cdot \mathbf{n} \right) + \frac{(\lambda^{j,\beta})^2}{2m_j^\beta} + \lambda^{j,\beta} \tilde{\mathbf{v}}^{j,\beta} \cdot \mathbf{n}. \quad (24)$$

Then, using the contact law (23) and defining

$$\tilde{\mathbf{v}}^{i,\alpha} = \sum_{\gamma|n_i^\gamma \in \sigma_i^\alpha} \chi^{i,\gamma} \tilde{\mathbf{v}}^{i,\gamma}, \quad \frac{1}{\mu_i^\alpha} = \sum_{\gamma|n_i^\gamma \in \sigma_i^\alpha} \frac{(\chi^{i,\gamma})^2}{m_i^\gamma}, \quad (25)$$

Equation (24) can be rewritten as

$$0 = \frac{(\lambda^{j,\beta})^2}{2} \left(\frac{1}{\mu_i^\alpha} + \frac{1}{m_j^\beta} \right) + \lambda^{j,\beta} (\tilde{\mathbf{v}}^{j,\beta} - \tilde{\mathbf{v}}^{i,\alpha}) \cdot \mathbf{n}. \quad (26)$$

This second order polynomial in $\lambda^{j,\beta}$ has a unique non-zero root

$$\lambda^{j,\beta} = 2 \frac{m_j^\beta \mu_i^\alpha}{m_j^\beta + \mu_i^\alpha} (\tilde{\mathbf{v}}^{i,\alpha} - \tilde{\mathbf{v}}^{j,\beta}) \cdot \mathbf{n}, \tag{27}$$

which gives the modulus and direction of the correction impulse on the node n_j^β on the meshfree body. The corresponding impulses on the finite element surface are easily obtained using Eq. (23). Remarkably, Eq. (27) has the same structure as the formula that computes the change of linear momentum in the collision between two point masses. The proposed algorithm, hence, can be thought of as solving the impact between the node n_j^β and a particle of mass μ_i^α and velocity $\tilde{\mathbf{v}}^{i,\alpha}$.

Physical arguments require that the impulses imparted to the nodes due to impact are all non-negative. In fact, for the model employed, Eq. (23) shows that it is sufficient to show that $\lambda^{j,\beta} \geq 0$. The inner product in Eq. (27) can be rewritten, with the aid of Eqs. (9) and (25), as

$$\begin{aligned} \mathbf{n} \cdot (\tilde{\mathbf{v}}^{i,\alpha} - \tilde{\mathbf{v}}^{j,\beta}) &= \frac{1}{\Delta t} \mathbf{n} \cdot \left(\sum_{\gamma | n_i^\gamma \in \sigma_i^\alpha} \chi^{i,\gamma} \tilde{\boldsymbol{\varphi}}^{i,\gamma} - \tilde{\boldsymbol{\varphi}}^{j,\beta} \right) \\ &\quad - \frac{1}{\Delta t} \mathbf{n} \cdot \left(\sum_{\gamma | n_i^\gamma \in \sigma_i^\alpha} \chi^{i,\gamma} \boldsymbol{\varphi}_n^{i,\gamma} - \boldsymbol{\varphi}_n^{j,\beta} \right). \end{aligned} \tag{28}$$

The first term on the right hand side can be further simplified to

$$\begin{aligned} \frac{1}{\Delta t} \mathbf{n} \cdot \left(\sum_{\gamma | n_i^\gamma \in \sigma_i^\alpha} \chi^{i,\gamma} \tilde{\boldsymbol{\varphi}}^{i,\gamma} - \tilde{\boldsymbol{\varphi}}^{j,\beta} \right) &= \frac{1}{\Delta t} \mathbf{n} \cdot (\boldsymbol{\varphi}_{n+1}^{j,\beta} - \tilde{\boldsymbol{\varphi}}^{j,\beta}) \\ &= \frac{|\boldsymbol{\varphi}_{n+1}^{j,\beta} - \tilde{\boldsymbol{\varphi}}^{j,\beta}|}{\Delta t}, \end{aligned} \tag{29}$$

which is, obviously, non-negative. The second term in Eq. (28) has an undetermined sign. When the contacting surfaces are smooth, it should be expected that the term in parenthesis does not differ much from \mathbf{n} , which is computed for the predictor, and that this term becomes non-negative. In the case of surfaces with corners, however, this need not be the case and it might result in numerical impulses that are in the opposite direction to the one expected. This is a side effect of the explicit integration, but one that rarely takes place. When it happens, it is always restricted to very small regions, and we accept it without any *ad hoc* correction.

4.5 Inelastic collisions

During inelastic collisions kinetic energy is not preserved and hence Eq. (20d) is not verified. Instead, a different relation

needs to be provided to relate the velocities of the impacting nodes, plus one extra equation that accounts for the energy loss. A common choice is a linear equation that determines a ratio of the relative velocities between colliding particles. Using again the two-particle impact analogy, we propose this equation to be

$$(\mathbf{v}_{n+1}^{i,\alpha} - \mathbf{v}_{n+1}^{j,\beta}) \cdot \mathbf{n} = -e(\tilde{\mathbf{v}}^{i,\alpha} - \tilde{\mathbf{v}}^{j,\beta}) \cdot \mathbf{n}, \tag{30}$$

where $e \in [0, 1]$, is the coefficient of restitution and $\mathbf{v}_{n+1}^{i,\alpha}$ is defined, in analogy with the definition of equivalent predictor velocity in expression (25), as the vector

$$\mathbf{v}_{n+1}^{i,\alpha} = \sum_{\gamma | n_i^\gamma \in \sigma_i^\alpha} \chi^{i,\gamma} \mathbf{v}_{n+1}^{i,\gamma}. \tag{31}$$

In what follows, we have assumed that e is constant, and identical for all contacting points. More sophisticated contact models in which e is locally defined as a function of the material properties could be envisioned, and incorporated to the algorithm directly. Using Eqs. (20a)–(20c), (23) and (30), the correction impulse on the node n_j^β follows as

$$\lambda^{j,\beta} = (1 + e) \frac{m_j^\beta \mu_i^\alpha}{m_j^\beta + \mu_i^\alpha} (\tilde{\mathbf{v}}^{i,\alpha} - \tilde{\mathbf{v}}^{j,\beta}) \cdot \mathbf{n}. \tag{32}$$

When $e = 1$, we recover the energy-preserving solution given by Eq. (27); when $e = 0$, the dissipation in the projection step is maximum. To see this, let us define the dissipation $\mathcal{D} = \tilde{K} - K_{n+1}$ and employ Eq. (26) to obtain

$$\mathcal{D} = \lambda^{j,\beta} (\tilde{\mathbf{v}}^{i,\alpha} - \tilde{\mathbf{v}}^{j,\beta}) \cdot \mathbf{n} - \frac{(\lambda^{j,\beta})^2 \mu_i^\alpha + \lambda^{j,\beta}}{2 \mu_i^\alpha \lambda^{j,\beta}}. \tag{33}$$

Taking the derivative of this equation with respect to $\lambda^{j,\beta}$, and setting it equal to zero we can deduce that the dissipation has its maximum value when the impulse is

$$\lambda_{\max \mathcal{D}}^{j,\beta} = \frac{m_j^\beta \mu_i^\alpha}{m_j^\beta + \mu_i^\alpha} (\tilde{\mathbf{v}}^{i,\alpha} - \tilde{\mathbf{v}}^{j,\beta}) \cdot \mathbf{n}, \tag{34}$$

which is precisely the value obtained in Eq. (32) when $e = 0$. As a result, the maximum value of the dissipation in a frictionless but inelastic impact is:

$$\mathcal{D} = \frac{\mu_i^\alpha m_j^\beta}{2(\mu_i^\alpha + m_j^\beta)} \left((\tilde{\mathbf{v}}^{i,\alpha} - \tilde{\mathbf{v}}^{j,\beta}) \cdot \mathbf{n} \right)^2. \tag{35}$$

4.6 Friction models

Last, we consider potential frictional effects between the contacting bodies, allowing for contact impulses with both normal and tangential components. The governing equations of the problem are similar to Eqs. (18), but now the impulses should not be restricted to be parallel to the direction \mathbf{n} . The general discrete balance equations are thus

$$\mathbf{p}_{n+1}^{j,\beta} - \tilde{\mathbf{p}}^{j,\beta} = \mathbf{i}^{j,\beta}, \quad (36a)$$

$$\mathbf{p}_{n+1}^{i,\gamma} - \tilde{\mathbf{p}}^{i,\gamma} = \mathbf{i}^{i,\gamma}, \quad (36b)$$

$$\mathbf{p}_{n+1}^{j,\beta} + \sum_{\gamma | n_i^\gamma \in \sigma_i^\alpha} \mathbf{p}_{n+1}^{i,\gamma} = \tilde{\mathbf{p}}^{j,\beta} + \sum_{\gamma | n_i^\gamma \in \sigma_i^\alpha} \tilde{\mathbf{p}}^{i,\gamma}, \quad (36c)$$

$$\left(\mathbf{v}_{n+1}^{i,\alpha} - \mathbf{v}_{n+1}^{j,\beta} \right) \cdot \mathbf{n} = -e \left(\tilde{\mathbf{v}}^{i,\alpha} - \tilde{\mathbf{v}}^{j,\beta} \right) \cdot \mathbf{n}, \quad (36d)$$

where $\mathbf{i}^{j,\beta}$, $\mathbf{i}^{i,\gamma}$ are now the impulses on the nodes. The solution of this system can be more easily obtained if the first three equations are projected onto the direction \mathbf{n} , and later solved in the plane perpendicular to this vector. The three projections onto \mathbf{n} , together with Eq. (36d), are precisely the ones studied in Sect. 4.5 and yield the velocity updates in the \mathbf{n} direction.

The velocity updates in the plane orthogonal to \mathbf{n} require additional model equations. To introduce such a model, let us first define the projection

$$\Pi(\mathbf{v}) = \mathbf{v} - \mathbf{v}|_n \mathbf{n} = \mathbf{v} - (\mathbf{v} \cdot \mathbf{n})\mathbf{n}, \quad (37)$$

mapping an arbitrary vector \mathbf{v} onto the orthogonal complement to \mathbf{n} , and let $\tilde{\omega}^{i,\alpha}$ be the weighted velocity

$$\tilde{\omega}^{i,\alpha} = \frac{1}{M_i^\alpha} \sum_{\gamma | n_i^\gamma \in \sigma_i^\alpha} m_i^\gamma \tilde{\mathbf{v}}^{i,\gamma}, \quad (38)$$

with M_i^α being the total mass of the nodes in σ_i^α . In the orthogonal complement to \mathbf{n} , let us define the unit vectors

$$\boldsymbol{\tau} = \frac{\Pi(\tilde{\mathbf{v}}^{j,\beta} - \tilde{\omega}^{i,\alpha})}{|\Pi(\tilde{\mathbf{v}}^{j,\beta} - \tilde{\omega}^{i,\alpha})|}, \quad \boldsymbol{\xi} = \boldsymbol{\tau} \times \mathbf{n}. \quad (39)$$

To model the frictional effects, first, we decompose the nodal impulses on the tangential directions $\boldsymbol{\xi}$ and $\boldsymbol{\tau}$ as in:

$$\Pi(\mathbf{i}^{j,\beta}) = -\eta^{j,\beta} \boldsymbol{\tau} - \rho^{j,\beta} \boldsymbol{\xi}, \quad \Pi(\mathbf{i}^{i,\gamma}) = \eta^{i,\gamma} \boldsymbol{\tau} + \rho^{i,\gamma} \boldsymbol{\xi}, \quad (40)$$

where $\eta^{j,\beta}$, $\rho^{j,\beta}$ are nonnegative scalars and $\eta^{i,\gamma}$, $\rho^{i,\gamma}$ distribute the impulse among the contacting nodes. Second, some additional relations must be provided among the tangential and normal impulses. Assuming a simple

Coulomb law with constant friction coefficient μ , the tangential impulse on the node must satisfy

$$0 \leq \sqrt{(\eta^{j,\beta})^2 + (\rho^{j,\beta})^2} \leq \mu \lambda^{j,\beta}. \quad (41)$$

Finally, the two possible contact types, namely *stick* or *slip* contact, must be distinguished, and modeled accordingly.

During *stick* contact there is no sliding in the tangential direction between the node n_j^β and the surface σ_i^α , and to enforce this condition we assume the simplifying relation

$$\Pi(\mathbf{v}_{n+1}^{i,\gamma}) = \Pi(\mathbf{v}_{n+1}^{j,\beta}), \quad (42)$$

for all nodes $n_i^\gamma \in \sigma_i^\alpha$. In this situation, the system of equations that governs the tangential contact update is

$$\Pi(\mathbf{p}_{n+1}^{j,\beta} - \tilde{\mathbf{p}}^{j,\beta}) = -\eta^{j,\beta} \boldsymbol{\tau} - \rho^{j,\beta} \boldsymbol{\xi}, \quad (43a)$$

$$\Pi(\mathbf{p}_{n+1}^{i,\gamma} - \tilde{\mathbf{p}}^{i,\gamma}) = \eta^{i,\gamma} \boldsymbol{\tau} + \rho^{i,\gamma} \boldsymbol{\xi}, \quad (43b)$$

$$\begin{aligned} \Pi(\mathbf{p}_{n+1}^{j,\beta}) + \sum_{\gamma | n_i^\gamma \in \sigma_i^\alpha} \Pi(\mathbf{p}_{n+1}^{i,\gamma}) &= \Pi(\tilde{\mathbf{p}}^{j,\beta}) \\ &+ \sum_{\gamma | n_i^\gamma \in \sigma_i^\alpha} \Pi(\tilde{\mathbf{p}}^{i,\gamma}), \end{aligned} \quad (43c)$$

$$\frac{\Pi(\mathbf{p}_{n+1}^{j,\beta})}{m_j^\beta} = \frac{\Pi(\mathbf{p}_{n+1}^{i,\gamma})}{m_i^\gamma}. \quad (43d)$$

A simple algebraic manipulation gives

$$\eta^{j,\beta} = \frac{m_j^\beta M_i^\alpha}{m_j^\beta + M_i^\alpha} \left(\tilde{\mathbf{v}}^{j,\beta} - \tilde{\omega}^{i,\alpha} \right) \cdot \boldsymbol{\tau}, \quad (44)$$

which is always non-negative and $\rho^{j,\beta}$

$$\rho^{j,\beta} = \frac{m_j^\beta M_i^\alpha}{m_j^\beta + M_i^\alpha} \left(\tilde{\mathbf{v}}^{j,\beta} - \tilde{\omega}^{i,\alpha} \right) \cdot \boldsymbol{\xi} = 0, \quad (45)$$

due to the orthonormality of $\boldsymbol{\tau}$ and $\boldsymbol{\xi}$. Combining the last expressions with Eq. (32), the *stick* condition can be rewritten as

$$\frac{M_i^\alpha}{m_j^\beta + M_i^\alpha} \left(\tilde{\mathbf{v}}^{j,\beta} - \tilde{\omega}^{i,\alpha} \right) \cdot \boldsymbol{\tau} \leq \frac{\mu_i^\alpha}{m_j^\beta + \mu_i^\alpha} \mu (1 + e) \left(\tilde{\mathbf{v}}^{i,\alpha} - \tilde{\mathbf{v}}^{j,\beta} \right) \cdot \mathbf{n}, \quad (46)$$

which, conveniently, only depends on quantities evaluated at the predictor step. Using it, we can decide, explicitly, whether the tangential motion during the update is going to involve sliding or not.

If, however, *slip* takes place, $\eta^{j,\beta} = \mu\lambda^{j,\beta}$, and the model is completed by apportioning the impulse on the element nodes proportionally to their masses, that is,

$$\eta^{i,\gamma} = \frac{m_i^\gamma}{M_i^\alpha} \eta^{j,\beta}, \quad \rho^{i,\gamma} = \frac{m_i^\gamma}{M_i^\alpha} \rho^{j,\beta}, \quad (47)$$

and by continuity between stick and slip contact we assume $\rho^{j,\beta} = 0$.

To conclude, it is useful to look at the balance of energy during the projection step, and verify that indeed the update defined for frictional contact in the tangential direction produces non-negative dissipation. To see this, we first note that the kinetic energy of the contacting entities at the corrected step can be expressed as a function of the velocities at the predicted step and impulses in the normal and tangential direction. Combining the velocity updates of Eqs. (18) and (40) we can write the kinetic energy at the corrected step as

$$K_{n+1} = \sum_{\gamma|n_i^\gamma \in \sigma_i^\alpha} \frac{m_i^\gamma}{2} \left| \tilde{\mathbf{v}}^{i,\gamma} - \frac{\chi^{i,\gamma} \lambda^{j,\beta}}{m_i^\gamma} \mathbf{n} + \frac{\eta^{i,\gamma}}{m_i^\gamma} \boldsymbol{\tau} + \frac{\rho^{i,\gamma}}{m_i^\gamma} \boldsymbol{\xi} \right|^2 + \frac{m_j^\beta}{2} \left| \tilde{\mathbf{v}}^{j,\beta} + \frac{\lambda^{j,\beta}}{m_j^\beta} \mathbf{n} - \frac{\eta^{j,\beta}}{m_j^\beta} \boldsymbol{\tau} - \frac{\rho^{j,\beta}}{m_j^\beta} \boldsymbol{\xi} \right|^2. \quad (48)$$

For the case of *stick* frictional contact, the dissipation $\mathcal{D} = \tilde{K} - K_{n+1}$ can be found to be

$$\begin{aligned} \mathcal{D} = & \lambda^{j,\beta} \tilde{\mathbf{v}}^{i,\alpha} \cdot \mathbf{n} - \frac{(\lambda^{j,\beta})^2}{2\mu_i^\alpha} - \frac{(\lambda^{j,\beta})^2}{2m_j^\beta} - \lambda^{j,\beta} \tilde{\mathbf{v}}^{j,\beta} \cdot \mathbf{n} \\ & - \sum_{\gamma|n_i^\gamma \in \sigma_i^\alpha} \eta^{i,\gamma} \tilde{\mathbf{v}}^{i,\gamma} \cdot \boldsymbol{\tau} - \frac{1}{2} \sum_{\gamma|n_i^\gamma \in \sigma_i^\alpha} \frac{(\eta^{i,\gamma})^2}{m_i^\gamma} \\ & - \frac{(\eta^{j,\beta})^2}{2m_j^\beta} + \eta^{j,\beta} \tilde{\mathbf{v}}^{j,\beta} \cdot \boldsymbol{\tau} - \sum_{\gamma|n_i^\gamma \in \sigma_i^\alpha} \rho^{i,\gamma} \tilde{\mathbf{v}}^{i,\gamma} \cdot \boldsymbol{\xi} \\ & - \frac{1}{2} \sum_{\gamma|n_i^\gamma \in \sigma_i^\alpha} \frac{(\rho^{i,\gamma})^2}{m_i^\gamma}, \end{aligned} \quad (49)$$

where the first line of the right-hand side of the equation above corresponds to Eq. (33) and is non-negative for the value $\lambda^{j,\beta}$ in Eq. (32). The rest of the right-hand side is the energy dissipated due to the frictional contact, namely $\mathcal{D}_\tau + \mathcal{D}_\xi$, and can be elaborated to

$$\begin{aligned} \mathcal{D}_\tau = & \sum_{\gamma|n_i^\gamma \in \sigma_i^\alpha} \frac{1}{2} m_i^\gamma (\tilde{\mathbf{v}}^{i,\gamma} \cdot \boldsymbol{\tau})^2 - \frac{1}{2} M_i^\alpha (\tilde{\mathbf{v}}^{j,\beta} \cdot \boldsymbol{\tau})^2 \\ & - \frac{M_i^\alpha (\eta^{j,\beta})^2}{2(m_j^\beta)^2} + \frac{\eta^{j,\beta} M_i^\alpha}{m_j^\beta} (\tilde{\mathbf{v}}^{j,\beta} \cdot \boldsymbol{\tau}) \\ & + \eta^{j,\beta} (\tilde{\mathbf{v}}^{j,\beta} \cdot \boldsymbol{\tau}) - \frac{(\eta^{j,\beta})^2}{2m_j^\beta}, \end{aligned} \quad (50)$$

where we have employed that

$$\eta^{i,\gamma} = m_i^\gamma \left(\frac{-\eta^{j,\beta}}{m_j^\beta} + \tilde{\mathbf{v}}^{j,\beta} \cdot \boldsymbol{\tau} - \tilde{\mathbf{v}}^{i,\gamma} \cdot \boldsymbol{\tau} \right). \quad (51)$$

By Jensen's inequality,

$$\frac{M_i^\alpha}{2} (\tilde{\boldsymbol{\omega}}^{i,\alpha} \cdot \boldsymbol{\tau})^2 \leq \sum_{\gamma|n_i^\gamma \in \sigma_i^\alpha} \frac{1}{2} m_i^\gamma (\tilde{\mathbf{v}}^{i,\gamma} \cdot \boldsymbol{\tau})^2, \quad (52)$$

and thus, using Eq. (44),

$$\mathcal{D}_\tau \geq \frac{m_j^\beta M_i^\alpha}{2(m_j^\beta + M_i^\alpha)} \left((\tilde{\boldsymbol{\omega}}^{i,\alpha} - \tilde{\mathbf{v}}^{j,\beta}) \cdot \boldsymbol{\tau} \right)^2, \quad (53)$$

which is non-negative. Similarly we can obtain that $\mathcal{D}_\xi \geq 0$ where we have employed that

$$\rho^{i,\gamma} = m_i^\gamma \left(\tilde{\mathbf{v}}^{j,\beta} \cdot \boldsymbol{\xi} - \tilde{\mathbf{v}}^{i,\gamma} \cdot \boldsymbol{\xi} \right), \quad (54)$$

using Eq. (43). For the case of slip contact, the dissipation in the correction step is now

$$\begin{aligned} \mathcal{D} = & \lambda^{j,\beta} \tilde{\mathbf{v}}^{i,\alpha} \cdot \mathbf{n} - \mu \lambda^{j,\beta} \tilde{\boldsymbol{\omega}}^{i,\alpha} \cdot \boldsymbol{\tau} - \lambda^{j,\beta} \tilde{\mathbf{v}}^{j,\beta} \cdot \mathbf{n} \\ & + \mu \lambda^{j,\beta} \tilde{\mathbf{v}}^{j,\beta} \cdot \boldsymbol{\tau} - \frac{(\lambda^{j,\beta})^2}{2} \left(\frac{1}{\mu_i^\alpha} + \frac{\mu^2}{M_i^\alpha} + \frac{1 + \mu^2}{m_j^\beta} \right). \end{aligned} \quad (55)$$

This is a parabola on the non-negative scalar $\lambda^{j,\beta}$, and evaluates to a non-negative dissipation as long as $\lambda^{j,\beta} \in (0, \lambda_{\mathcal{D}=0}^{j,\beta})$ where $\lambda_{\mathcal{D}=0}^{j,\beta}$ is

$$\lambda_{\mathcal{D}=0}^{j,\beta} = 2 \frac{(\tilde{\mathbf{v}}^{i,\alpha} - \tilde{\mathbf{v}}^{j,\beta}) \cdot \mathbf{n} + \mu (\tilde{\mathbf{v}}^{j,\beta} - \tilde{\boldsymbol{\omega}}^{i,\alpha}) \cdot \boldsymbol{\tau}}{\frac{1}{\mu_i^\alpha} + \frac{\mu^2}{M_i^\alpha} + \frac{1 + \mu^2}{m_j^\beta}}. \quad (56)$$

Employing Eq. (46) to find the limit value, the dissipation can be re-written as

$$\lambda_{\mathcal{D}=0}^{j,\beta} = 2 \frac{(\tilde{\mathbf{v}}^{i,\alpha} - \tilde{\mathbf{v}}^{j,\beta}) \cdot \mathbf{n}}{\frac{1}{\mu_i^\alpha} + \frac{\mu^2}{M_i^\alpha} + \frac{1 + \mu^2}{m_j^\beta}} \left(1 + \mu^2 (1 + e) \frac{\mu_i^\alpha (m_j^\beta + M_i^\alpha)}{M_i^\alpha (m_j^\beta + \mu_i^\alpha)} \right). \quad (57)$$

But this limit value can be bounded from below since

$$\begin{aligned} \lambda_{\mathcal{D}=0}^{j,\beta} & \geq 2 \frac{(\tilde{\mathbf{v}}^{i,\alpha} - \tilde{\mathbf{v}}^{j,\beta}) \cdot \mathbf{n}}{\frac{1}{\mu_i^\alpha} + \frac{1}{m_j^\beta}} \\ & \geq (1 + e) \frac{\mu_i^\alpha m_j^\beta}{\mu_i^\alpha + m_j^\beta} (\tilde{\mathbf{v}}^{i,\alpha} - \tilde{\mathbf{v}}^{j,\beta}) \cdot \mathbf{n} = \lambda^{j,\beta}, \end{aligned} \quad (58)$$

where the last identity follows Eq. (32). We conclude that $0 \leq \lambda^{j,\beta} \leq \lambda_{\mathcal{D}=0}^{j,\beta}$ and thus the energy dissipation is also non-negative in the slip case.

4.7 Relation of the proposed algorithm with existing methods

The most commonly employed methods for dealing with contacting surfaces in explicit dynamics start from the definition of a *gap* function g that gauges the distance between interacting bodies. Numerical methods are designed to keep this function larger than or equal to zero and, potentially, to impose forces in the direction of its gradient in order to prevent it from becoming negative (see, for example, [4]).

Numerical methods of the type referred to impose the balance of linear momentum as in

$$\mathbf{p}_{n+1}^{a,b} - \tilde{\mathbf{p}}^{a,b} = \lambda \frac{\partial g(\Phi_n)}{\partial \varphi^{a,b}} \quad a = \{i, j\}, b = \{\gamma | n_i^\gamma \in \sigma_i^\alpha, \beta\}, \tag{59}$$

with $\lambda = \kappa g(\Phi_n)$, and κ a penalty constant. To reveal the relation between these methods and the one presented in this article let us consider the *gap* function

$$g(\{\varphi^{i,\gamma}\}_{\gamma | n_i^\gamma \in \sigma_i^\alpha}, \varphi^{j,\beta}) = \left\langle \mathbf{n}, \varphi^{j,\beta} - \sum_{\gamma | n_i^\gamma \in \sigma_i^\alpha} \chi^{i,\gamma} \varphi^{i,\gamma} \right\rangle \tag{60}$$

where $\chi^{i,\gamma}$ are the scalar coefficients defined in Eq. (22), with node n_β^j in the meshfree body and nodes n_i^γ on the face σ_i^α of a finite element mesh.

First, we note that the sum over nodes on the element face σ_i^α is a convex combination that results in a point inside the face. This shows that the function (60) is just measuring the (signed) distance of the node n_β^j to the surface σ_i^α , and thus it seems a potentially useful *gap* function. But second, a straightforward calculation reveals that the impulse equations (59) are precisely Eq.(18a), for the node n_β^j , and Eqs. (18b) for the nodes $n_i^\gamma \in \sigma_i^\alpha$. Hence we conclude that the algorithms developed herein, at least for the normal component, are just a particular instance of *gap*-driven contact methods, in which the *gap* function is given by Eq. (60). Finally, we note that the method proposed in the current work replaces the penalty form of the impulse λ with the prediction/correction algorithm.

The structure and sequence of computations in the contact algorithms presented in this section is summarized in the Appendix as a flowchart.

5 Simulations

In this section we illustrate the performance of the proposed contact algorithm on a set of selected examples that involve,

at least, one body discretized with finite elements and another with a meshless method. To keep the computations as simple as possible, and focus on the features of the contact interaction, all finite element meshes consist of four-node tetrahedra. While the use of hexahedra or higher order elements involve no theoretical complexity, the detection of penetration and the projection steps become much more involved.

5.1 Double elastic bar impact

In this test we analyze the elastic impact of two identical rods against each other. The cylinders have radius and length equal to 3.2 mm and 32.4 mm, respectively. One of the rods is discretized with finite elements and the other is discretized with a meshfree method, with symmetry conditions employed in both cases restricting the analysis to one-quarter of the domain. The finite element and the meshfree bodies use, respectively, 798 and 1093 nodes. The material of the rods is hyperelastic and a neo-hookean model is employed with Young’s modulus $E = 117$ GPa, Poisson’s ratio $\nu = 0.35$, and density 8930 kg/m³. The rods are launched at 113.5 m/s against each other and compression waves are originated in both bodies when they come into contact. These waves travel back as release waves causing the bodies to separate, eventually. See Fig. 3 for an illustration.

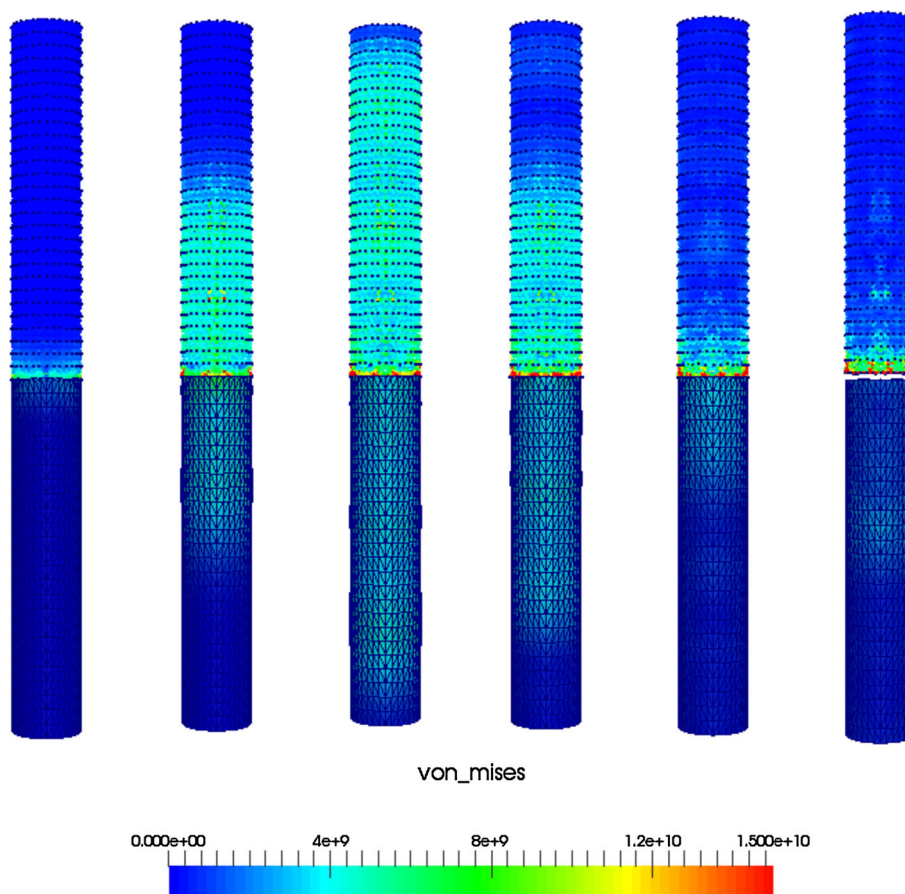
This example shows that the proposed contact algorithm is able to deal with high velocity impacts of finite elements/meshfree discretizations in a robust way, without the need to adjust any penalty parameter. As a result, not only the definition of the contact properties is simplified, but also it has no influence whatsoever in the critical time step size.

5.2 High velocity impact of a sphere with a deformable plate

As hinted at in the introduction, high velocity impacts are one of the most common applications of combined finite elements/meshfree methods, especially when one of the interacting bodies (typically the impactor) suffers large distortions, even fracture. In the following example we explore a situation of this type, and consider the frictionless and elastic impact between a deformable sphere and an elastic plate. The simulation illustrates the ability of the method to model a very large number of impacting “particles”, allowing a very robust simulation of fragmentation.

The sphere of the example has a radius of 25 mm, it is launched towards the plate with a velocity of 300 m/s in the normal direction, and is discretized with a meshfree method, employing 189 nodes. For high velocity impacts such as the one under consideration, it is often decided that the impactor behaves like a compressible fluid, breaking for any negative

Fig. 3 Double Taylor bar impact, Von Mises stress (Pa). From left to right, solutions at time $t = 1, 5, 9, 12, 16, 21 \mu s$



pressure. In this simulation, the sphere is modeled with a fluid of dynamic viscosity $\nu = 0.1 \text{ Pa}\cdot\text{s}$, density $\rho = 3000 \text{ kg/m}^3$, and a linear equation of state with bulk modulus $K = 5 \text{ GPa}$. The plate has dimensions $0.01 \times 0.15 \times 0.15 \text{ m}^3$ and is discretized with a finite element model of 512 nodes, with all the displacements of the lateral surfaces constrained. The material of the plate is neo-hookean, with Young's modulus $E = 1 \text{ GPa}$, Poisson's ratio $\nu = 0.33$, and density $\rho = 1740 \text{ kg/m}^3$. The evolution of the von Mises stress is plotted in Fig. 4, where the fragmentation of the (meshfree) sphere can be observed. The vertical reaction of the plate supports, as a function of time, is depicted in Fig. 5. As a result of the vibrations induced on the plate, the maximum upwards reaction takes place at approximately $150 \mu s$, followed by a reversal of the sign of this force. During the impact, the sphere breaks into many small pieces, and each of them continues to interact with the plate. The contact algorithm, without any additional modification, deals with the new surface interactions. Remarkably, the reaction force changes smoothly in time, without the high frequency oscillations that often appear in penalty-based contact solutions. The integration algorithm does not employ artificial numerical dissipation, and this smoothness is rather the result of the lack of large penalty parameters in the numerical model.

5.3 Sliding block on an inclined plane

The sliding of a deformable neo-hookean cube of side with length 0.03 m with Young's modulus of value 70 GPa and Poisson's ratio 0.33 , along a rigid plane with an inclination of $\alpha = 15^\circ$ is performed to assess the performance of the contact algorithm with friction. See Fig. 6 for an illustration. The contact considered is completely elastic ($e = 1$) and with a friction coefficient $\mu = 0.1$. The density of the sliding box is 2800 kg/m^3 and gravity has been set to the value $g = 2000 \text{ m/s}^2$ to reduce the simulation time. The cube has been discretized with a meshfree method, employing 125 nodes, while the motion of the plane is completely constrained. The analytical solution for the acceleration of a sliding cube is

$$a_{\text{plane}} = g(\sin(\alpha) - \mu \cos(\alpha)). \tag{61}$$

Since the acceleration is constant, the kinetic energy of the cube, given its total mass m , is

$$K = \frac{1}{2}m(a_{\text{plane}} t)^2. \tag{62}$$

This solution is compared in Fig. 7 with the kinetic energy in the simulation, and proves that the frictional contact algo-

Fig. 4 Von Mises stress (Pa) of the sphere impact with deformable plate. From left to right, top to bottom, solutions at time $t = 5, 32, 80, 132, 200, 302 \mu\text{s}$

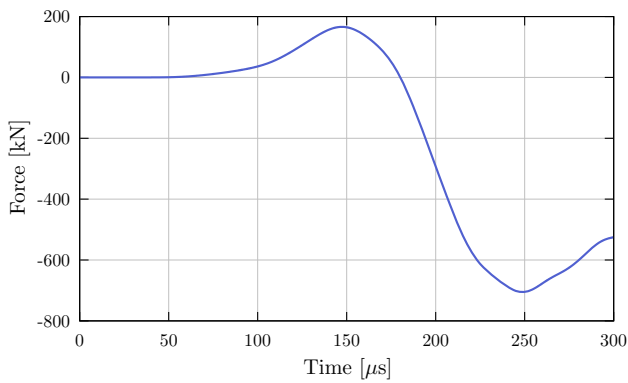
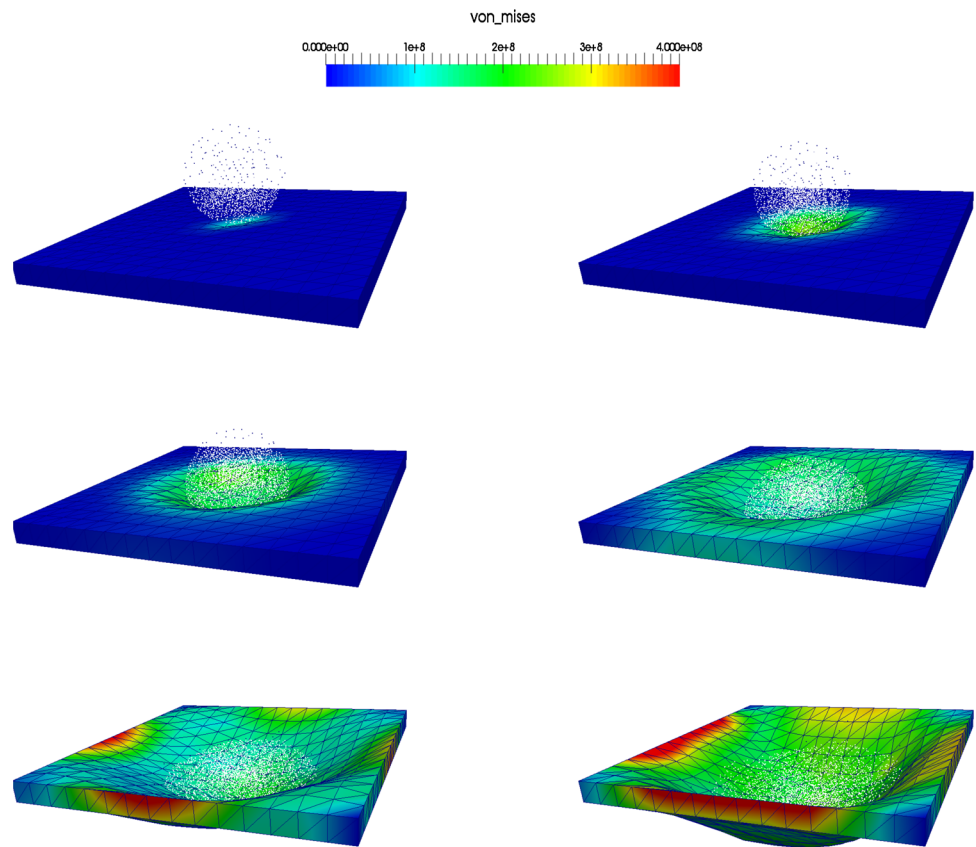


Fig. 5 Normal force exerted on the plate

rithm captures accurately the global motion of the sliding block.

5.4 Multi-body impact

A multi-body simulation is performed with elastic contact among deformable bodies. All of the latter are cubes of volume 0.03^3 m^3 , two of them discretized with a meshfree method, and another three with finite element meshes. The cubes are set at the beginning of the simulation with their edges aligned with the coordinate axes. The meshfree

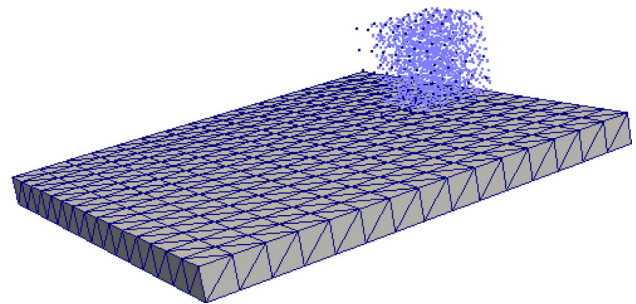


Fig. 6 Meshfree cube on inclined plane

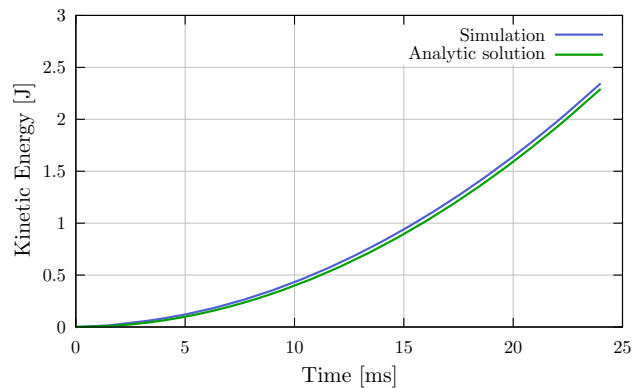


Fig. 7 Kinetic energy of the sliding cube on an inclined plane

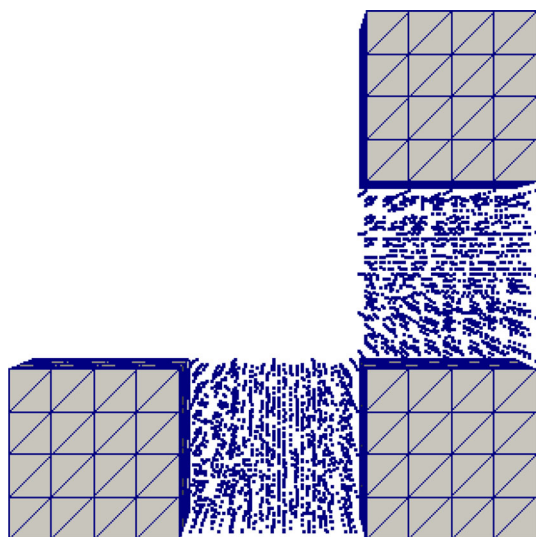


Fig. 8 Arrangement of finite element/meshfree cubes

bodies have their centers of mass at the points $(0, 0, 0)$ m and $(0, 0.0315, 0.0315)$ m. The centers of mass of the three finite element cubes are, respectively, placed initially at the points $(0, 0.0315, 0.063)$ m, $(0, -0.0315, 0)$ m and $(0, 0.0315, 0)$ m (see Fig. 8 for an illustration). All the bodies employ the same neo-hookean material with Young’s modulus 71 GPa, Poisson’s ratio 0.33 and density 2800 kg/m^3 . The finite element and meshfree cubes are discretized with 125 nodes. An initial velocity $(25.0, -120.0, 100.0)$ m/s is applied to the cube whose center of mass has position $(0, 0.0315, 0)$, setting up its motion and, due to the contact forces, the motion of all remaining cubes.

Figure 9 shows the evolution of the linear momentum, which remains constant at all times. This is due to the fact that the standard central difference method preserves the linear momentum, and that the contact algorithm is designed to preserve it during the projection step. Figure 10 depicts the energy evolution, whose oscillations can be attributed to both the central difference scheme and the contact interactions. Finally, the evolution of von Mises stress on the cubes is shown in Fig. 11, where the large motions of all the bodies can be observed.

5.5 Taylor’s bar impact

We study next Taylor’s high velocity anvil impact [29], an experiment for which there exists a wealth of experimental data and is often employed to study the rate dependent elastoplastic behavior of materials and the ability of algorithms to capture it [30,31]. Taylor’s test consists of a metallic cylinder launched at high velocity against a wall or plate. When one of the flat surfaces of the cylinder impacts, the specimen deforms plastically and its final shape—which conserves the axial symmetry—can be measured easily.

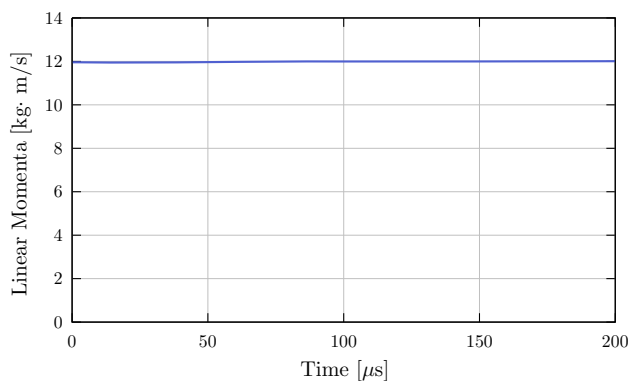


Fig. 9 Linear momenta evolution for multi-body impact

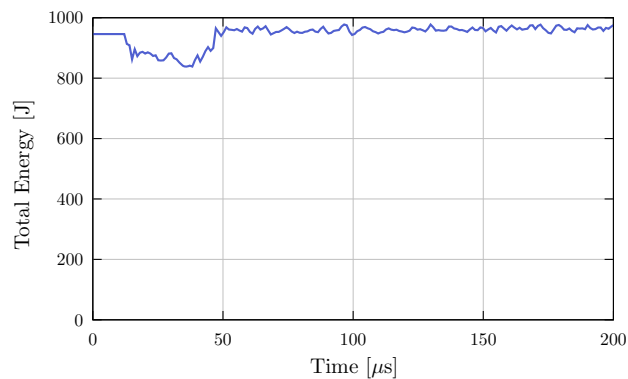


Fig. 10 Total energy evolution for multi-body impact

One of the constitutive laws that is often employed to model metals with rate- and temperature-dependent elastoplastic behavior is Johnson–Cook’s [32]. This J_2 model employs a yield stress of the form

$$\sigma_y = (A + B\epsilon^N) \left(1 + C \log \frac{\dot{\epsilon}}{\epsilon_0} \right) \left(1 - \left(\frac{T - T_0}{T_m - T_0} \right)^M \right). \tag{63}$$

In this expression, ϵ is the accumulated plastic strain, $\dot{\epsilon}$ its rate, and T , T_m and T_0 are, respectively, the current, melting, and reference temperatures of the material. The parameters A , B , N , M , ϵ_0 are material constants that, together with Lamé parameters λ and μ , completely determine the response of the material.

Based on this test, we analyze next the impact of a copper cylinder launched onto a wall at 227 m/s [30,32,33]. The parameters of the Johnson–Cook’s model are given in Table 1. The density is taken to be $\rho = 8960 \text{ kg/m}^3$ and the Lamé elastic constants are $\lambda = 150 \times 10^3 \text{ MPa}$, $\mu = 75 \times 10^3 \text{ MPa}$. The simulation assumes isothermal conditions at temperature $T = 300 \text{ K}$ and the anvil initial diameter and length are, respectively, 7.62 mm and 25.4 mm.

In the simulation, the cylinder is placed 1.3mm away from the plate, which is considered to be completely rigid by con-

Fig. 11 Von Mises stress (Pa) for multi-body impact. From left to right, top to bottom, solutions at time $t = 19, 49, 79, 128, 295, 376 \mu\text{s}$

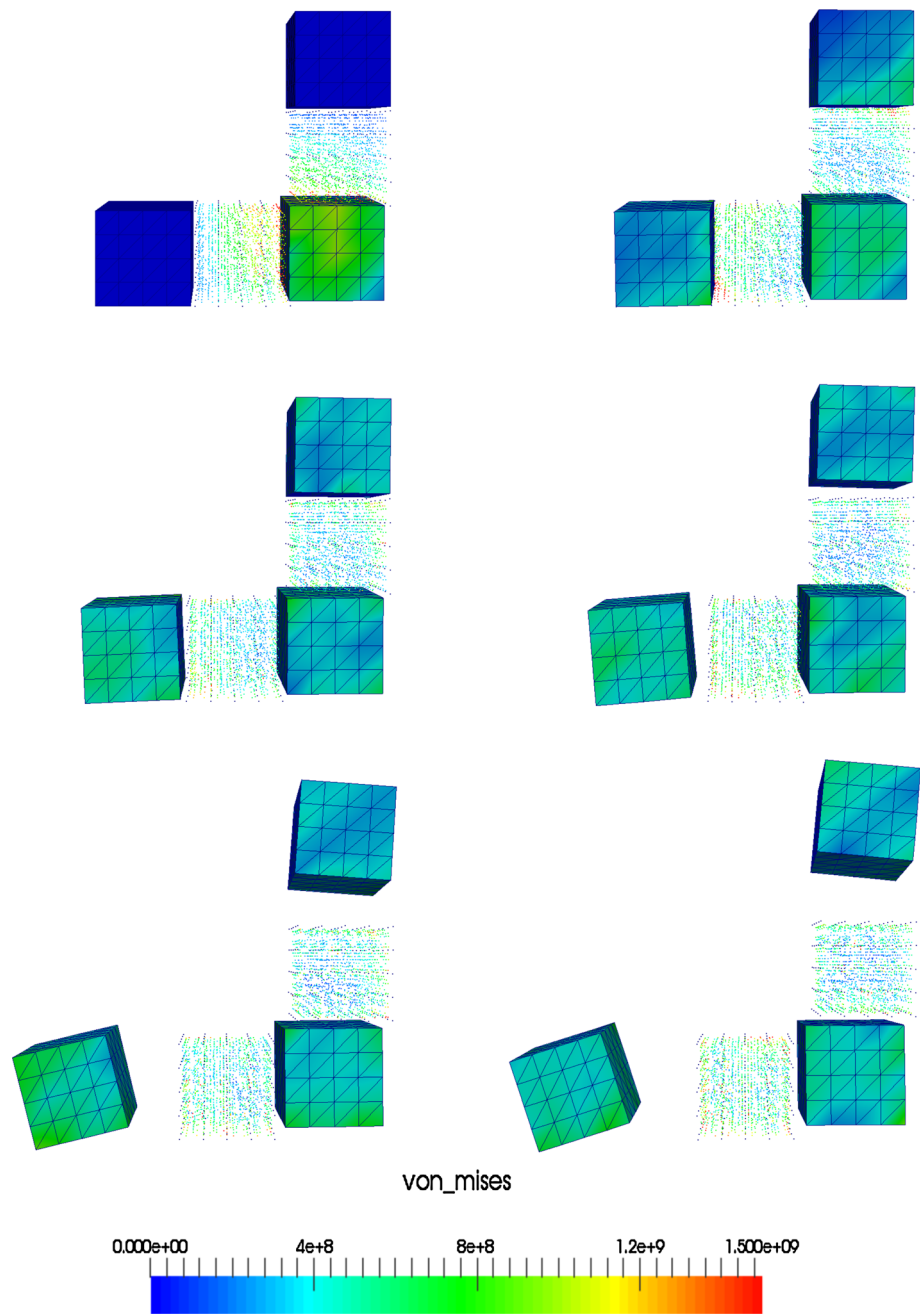


Table 1 Johnson–Cook constants for copper

A (MPa)	B (MPa)	C (–)	N (–)	M (–)	T_0 (K)	T_m (K)
90	292	0.025	0.31	1.09	300.0	1356.0

straining the displacements of all of its nodes. The Coulomb friction coefficient in the contact is assumed to be constant and equal to 0.1, and the restitution coefficient is taken to be zero, modeling a perfectly inelastic impact. Approximately 5.7 after the anvil is launched, it impacts the plate and starts deforming with large plastic deformations. Figure 12 shows

six snapshots of the simulations, illustrating the deformations in the model and the field of plastic slip. The figures depict this slip at the material points, and also shows in black the nodes in the finite element and meshfree bodies.

5.6 Oblique elastoplastic impact

In the last example, we consider the high-velocity, elastoplastic oblique impact with friction of a deformable sphere against a deformable plate as previously proposed in the literature [19]. The diameter of the sphere and the thickness of the plate are both equal to 6.4 mm. The other two dimensions

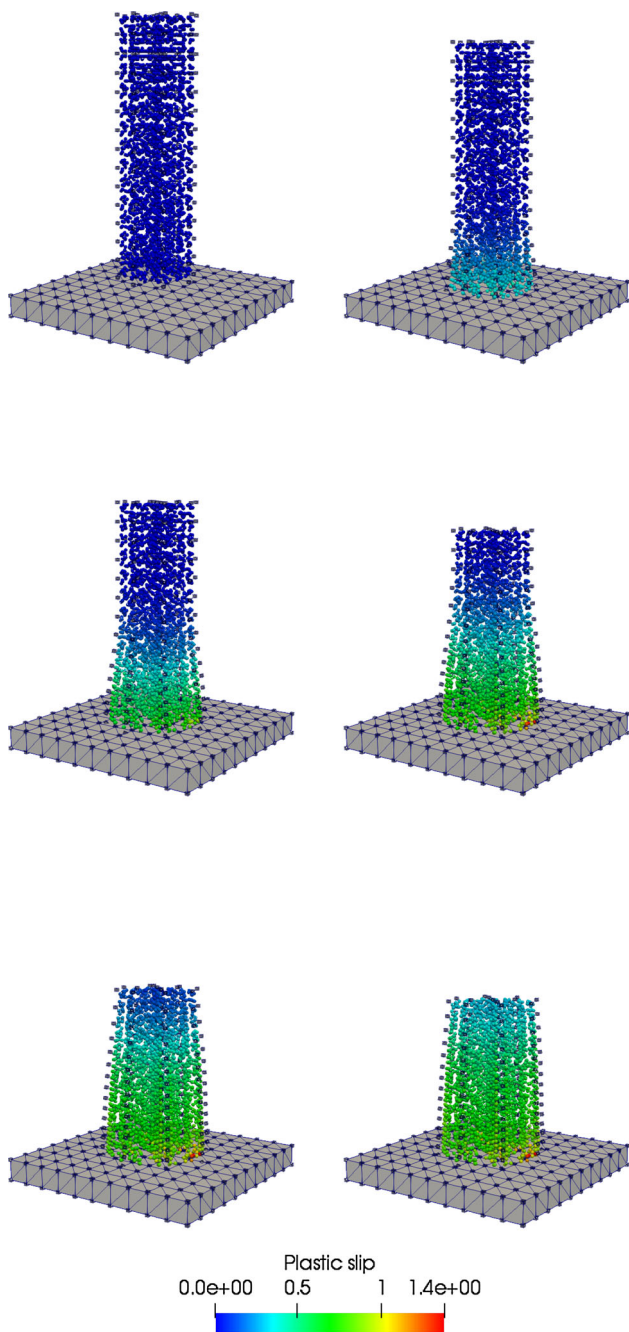


Fig. 12 Taylor's anvil test. From left to right, top to bottom, deformed configurations at time $t \sim 11.2 \cdot k$, with $k = 0, 1, \dots, 5$, showing the plastic slip evolution

of the plate are taken to be equal to 20 mm, in x direction, and 30 mm in y direction. See Fig. 13 for an illustration of the geometry and the definition of the coordinate axes. The sphere has an initial velocity of 700 m/s towards the plate with an angle of 0.35 rad with respect to the plate's surface.

The sphere and plate are both of steel. The former has the properties of S7 steel, whereas the latter is of type 4340. Both materials are modeled with a Johnson–Cook's law (see Eq. 63) with the data given for these two steels in their origi-

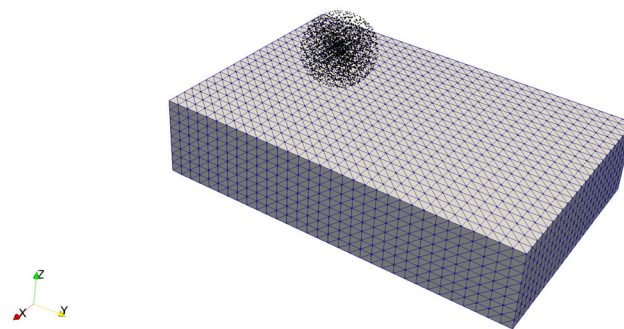


Fig. 13 Elastoplastic oblique impact of a sphere with a plate. Initial configuration, showing the finite element mesh and meshless body

nal article [32]. For convenience, these data are summarized in Table 2, including the density ρ . In addition, for both materials we have considered that Young's modulus is 210 GPa, Poisson's ratio is 0.3, and assumed isothermal conditions at 300 K.

The meshfree sphere includes 189 nodes and 3072 material points. The finite element model of the plate has approximately 37,000 elements and 7500 nodes. All the nodes on the lateral faces of the plate have their degrees of freedom constrained. The contact is completely elastic and Coulomb's friction coefficient is 0.05. Figure 14 shows six snapshots of the impact process, cutting the model by the symmetry plane perpendicular to the x axis. The figure illustrates the presence of plastic deformation in the finite element and meshfree bodies.

The evolution of the linear momentum and energy of the sphere are shown in Figs. 15 and 16, respectively. The first figure confirms a smooth change of momentum in both the normal and tangential directions to the plate. The second one illustrates the good energy control of the method during the contact phase. We note that no smoothing has been applied on any of the curves depicted.

6 Summary

We have presented a new algorithm for contact/impact in explicit simulations of deformable bodies. The proposed method has several salient features that make it very appealing for general purpose computations. First, it imposes very mild stability restrictions on the time step size employed in the integration. Second, it bypasses the need to choose a penalty parameter since the impenetrability constraint is not imposed with an artificial stiffness, but rather with a projection scheme. This has shown to produce reaction forces and momenta exchanges without spurious high frequency oscillations. Third, it possesses favorable energy estimates for contact with or without friction and/or perfect restitution. Fourth, it is asymmetric by construction, and thus can be employed for modeling interactions between finite element models, or between a finite element model and a meshfree one.

Table 2 Johnson–Cook constants for steels

Steel type	A (MPa)	B (MPa)	C (-)	N (-)	M (-)	T_0 (K)	T_m (K)	ρ (kg/m ³)
4340	792	510	0.014	0.26	1.03	300	1793	7830
S7	1539	447	0.012	0.18	1.00	300	1763	7750

Fig. 14 Impact of elastoplastic sphere. From left to right, top to bottom, deformed configurations at time $t \sim 4 \cdot k$, with $k = 0, 1, \dots, 5$, showing the plastic slip evolution and cut by the plane of symmetry

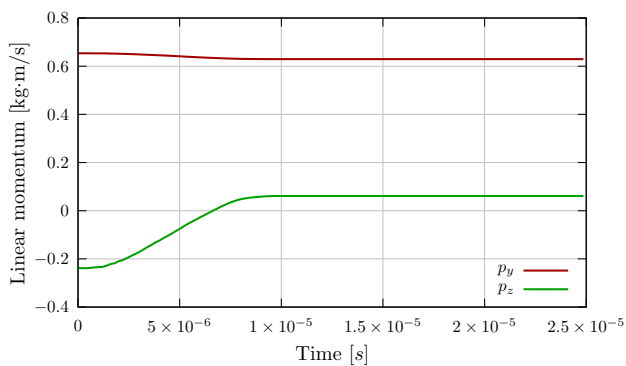
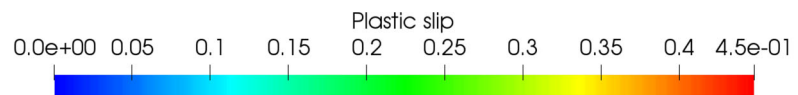
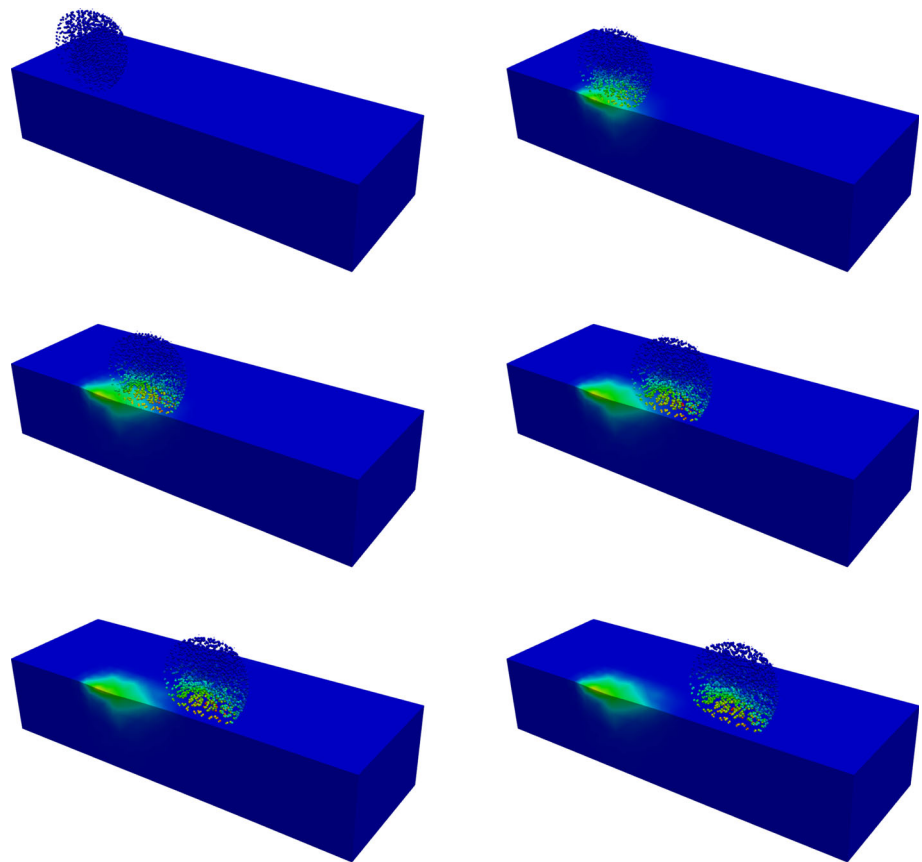


Fig. 15 Linear momentum components of the sphere during the impact of example 5.6

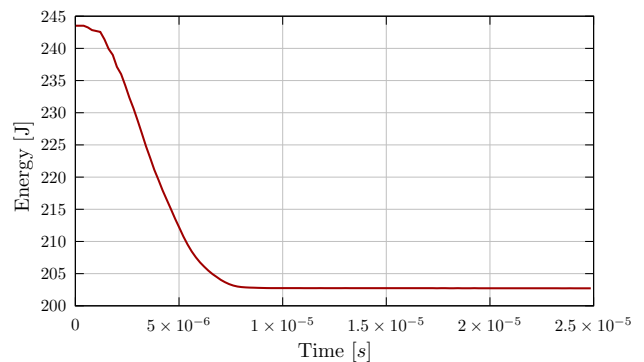


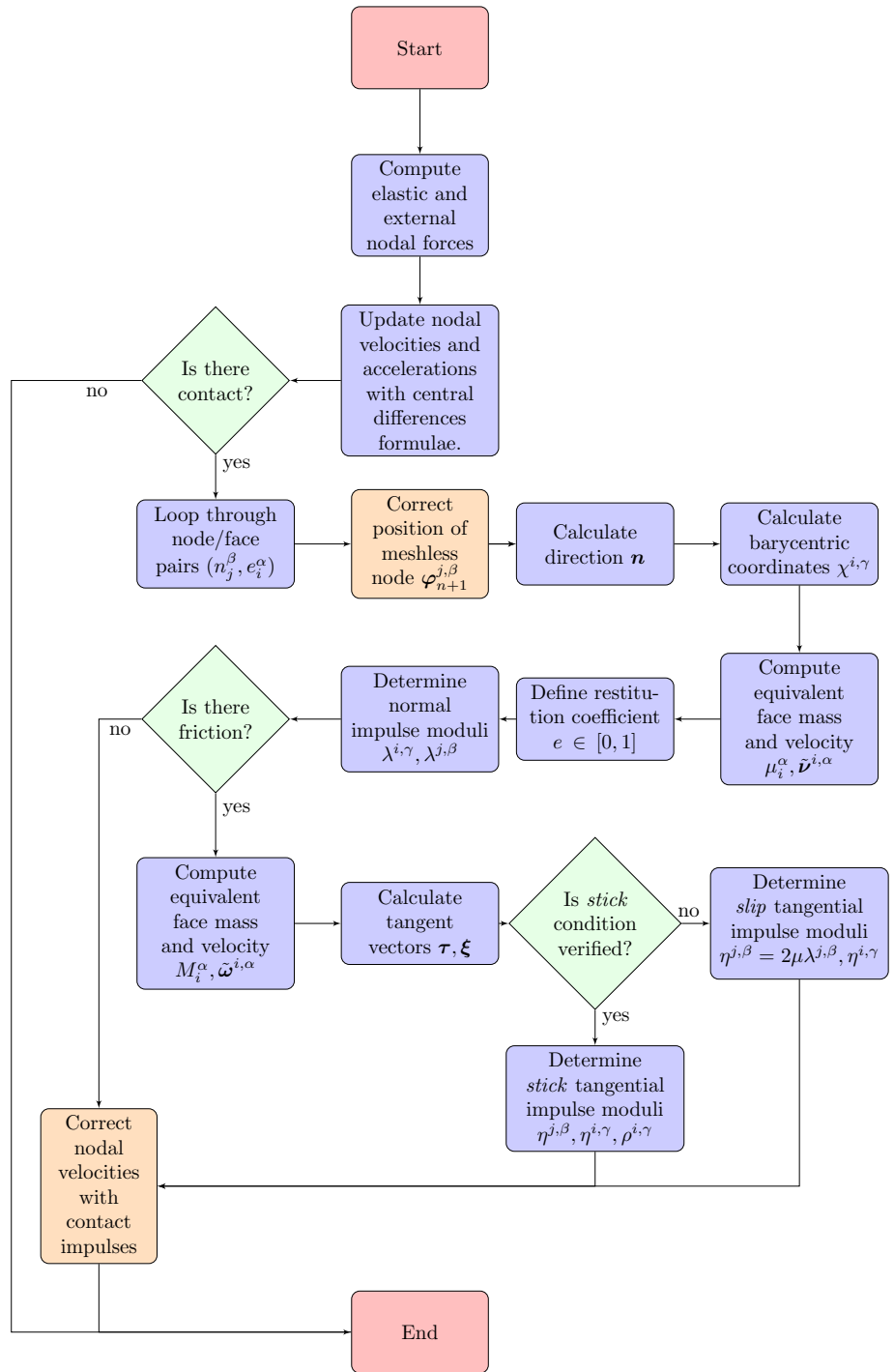
Fig. 16 Total energy of the sphere during the impact of example 5.6

Overall, the method is simple to implement, and extremely robust for all types of contact simulations, including those involving bodies with sharp edges or corners. We have illus-

Appendix: Flowchart

See Fig. 17.

Fig. 17 Flowchart of the dynamic update in one time step, including the contact algorithm



References

1. Zhong Z-H, Mackerle J (1992) Static contact problems—a review. *Eng Comput* 9(1):3–37
2. Zhong Z-H, Mackerle J (1994) Contact-impact problems: a review with bibliography. *Appl Mech Rev* 47(2):55
3. Bourago NG, Kukudzhanov VN (2005) A review of contact algorithms. *Mech Solids* 40(1):35–71
4. Laursen TA (2002) *Computational contact and impact mechanics*. Springer, Berlin
5. Wriggers P (2002) *Computational contact mechanics*. Wiley, New York
6. Goudreau GL, Hallquist JO (1982) Recent developments in large-scale finite element Lagrangian hydrocode technology. *Comput Methods Appl Mech Eng* 33:725–757
7. Hallquist JO, Goudreau GL, Benson DJ (1985) Sliding interfaces with contact-impact in large-scale Lagrangian computations. *Comput Methods Appl Mech Eng* 51(1–3):107–137
8. Wriggers P, Van Vu T, Stein E (1990) Finite element formulation of large deformation impact-contact problems with friction. *Comput Struct* 37:319–331
9. Carpenter NJ, Taylor RL, Katona MG (1991) Lagrange constraints for transient finite element surface contact. *Int J Numer Methods Eng* 32(1):103–128
10. Belytschko T, Neal MO (1991) Contact-impact by the pinball algorithm with penalty and Lagrangian methods. *Int J Numer Methods Eng* 31:547–572
11. Heinstein MW, Attaway SW, Swegle JW, Mello FJ (1992) A general purpose contact detection algorithm for nonlinear structural analysis codes. Technical Report SAND92-2141, Sandia National Lab
12. Malone JG, Johnson NL (1994) A parallel finite element contact/impact algorithm for non-linear explicit transient analysis: part I—the search algorithm and contact mechanics. *Int J Numer Methods Eng* 37(4):559–590
13. Heinstein MW, Mello FJ, Attaway SW, Laursen TA (2000) Contact-impact modeling in explicit transient dynamics. *Comput Methods Appl Mech Eng* 187:621–640
14. Malone JG, Johnson NL (1994) A parallel finite element contact/impact algorithm for non-linear explicit transient analysis: part II—parallel implementation. *Int J Numer Methods Eng* 37(4):591–603
15. Attaway SW, Hendrickson BA, Plimpton SJ, Gardner DR, Vaughan CT, Brown KH, Heinstein MW (1998) A parallel contact detection algorithm for transient solid dynamics simulations using PRONTO3D. *Comput Mech* 22:143–159
16. Brown K, Attaway S, Plimpton S, Hendrickson B (2000) Parallel strategies for crash and impact simulations. *Comput Methods Appl Mech Eng* 184:375–390
17. Taylor LM, Flanagan DP (1989) Pronto 3d: a three-dimensional transient solid dynamics program. Technical report, Sandia National Labs., Albuquerque
18. Zywicz E, Puso MA (1999) A general conjugate-gradient-based predictor–corrector solver for explicit finite-element contact. *Int J Numer Methods Eng* 44(4):439–459
19. Johnson GR, Stryk RA (2001) Symmetric contact and sliding interface algorithms for intense impulsive loading computations. *Comput Methods Appl Mech Eng* 190(35):4531–4549
20. Cirak F, West M (2005) Decomposition contact response (DCR) for explicit finite element dynamics. *Int J Numer Methods Eng* 64(8):1078–1110
21. Attaway SW, Heinstein MW, Swegle JW (1994) Coupling of smooth particle hydrodynamics with the finite element method. *Nucl Eng Des* 150(2):199–205
22. De Vuyst T, Vignjevic R, Campbell JC (2005) Coupling between meshless and finite element methods. *Int J Impact Eng* 31(8):1054–1064
23. Zhang Z, Qiang H, Gao W (2011) Coupling of smoothed particle hydrodynamics and finite element method for impact dynamics simulation. *Eng Struct* 33(1):255–264
24. Long T, Hu D, Yang G, Wan D (2016) A particle-element contact algorithm incorporated into the coupling methods of FEM-ISPH and FEM-WCSPH for FSI problems. *Ocean Eng* 123(C):154–163
25. Li S, Liu WK (2004) *Meshfree particle methods*. Springer, Berlin Heidelberg
26. Cueto E, Doblare M, Gracia L (2000) Imposing essential boundary conditions in the natural element method by means of density-scaled. *Int J Numer Methods Eng* 49:519–546
27. Arroyo M, Ortiz M (2006) Local maximum-entropy approximation schemes: a seamless bridge between finite elements and meshfree methods. *Int J Numer Methods Eng* 65:2167–2202
28. Huerta A, Fernández-Méndez S (2000) Enrichment and coupling of the finite element and meshless methods. *Int J Numer Methods Eng* 48(11):1615–1636
29. Taylor G (1948) The use of flat-ended projectiles for determining dynamic yield stress. I. Theoretical considerations. *Proc Math Phys Eng Sci* 194(1038):289–299
30. Whiffin AC (1948) The use of flat-ended projectiles for determining dynamic yield stress. II. Tests on various metallic materials. *Proc Math Phys Eng Sci* 194(1038):300–322
31. Brüning M, Driemeier L (2007) Numerical simulation of Taylor impact tests. *Int J Plast* 23(12):1979–2003
32. Johnson GR, Cook WH (1983) A constitutive model and data for metals subjected to large strains, high strain rates and high temperatures. In: 7th International conference on Ballistics, pp 541–547
33. Johnson GR, Cook WH (1985) Fracture characteristics of three metals subjected to various strains, strain rates, temperatures and pressures. *Eng Fract Mech* 21(1):31–48

Publisher's Note Springer Nature remains neutral with regard to jurisdictional claims in published maps and institutional affiliations.